ChemPubSoc Europe

DOI: 10.1002/cctc.201402897

CHEMCATCHEM Full Papers

Binder Effects in SiO_2- and Al_2O_3-Bound Zeolite ZSM-5-Based Extrudates as Studied by Microspectroscopy

Gareth T. Whiting,[a] Florian Meirer,[a] Machteld M. Mertens,[b] Anton-Jan Bons,[c] Brian M. Weiss,[d] Paul A. Stevens,[d] Emiel de Smit,[c] and Bert M. Weckhuysen*[a]

Microspectroscopic methods were explored to investigate binder effects occurring in ZSM-5-containing SiO_2- and Al_2O_3-bound millimetre-sized extrudates. Using thiophene as a selective probe for Brønsted acidity, coupled with time-resolved in situ UV/Vis and confocal fluorescence microspectroscopy, variations in reactivity and selectivity between the two distinct binder types were established. It was found that aluminium migration occurs in ZSM-5-containing Al_2O_3-bound extrudates, forming additional Brønsted acid sites. These sites strongly influence the oligomer selectivity, favouring the formation of thiol-like species (i.e., ring-opened species) in contrast to higher oligomers, predominantly formed on SiO_2-bound ZSM-5-containing extrudates. Not only were the location and distribution of these oligomers visualised by 3D analysis, it was also observed that more conjugated species appeared to grow off the surface of the zeolite ZSM-5 crystals (containing less conjugated species) into the surrounding binder material. Furthermore, a higher binder content resulted in an increasing overall reactivity owing to the greater number of stored thiophene monomers available per Brønsted acid site.

Introduction

Zeolite-based catalyst bodies are employed on a global scale in important chemical processes, such as the synthesis of many bulk chemicals[1,2] as well as crude-oil refining.[3,4] Particular examples include xylene isomerisation,[5,6] benzene alkylation[7,8] and methanol conversion to hydrocarbons.[9,10] Catalyst bodies, such as extrudates, have millimetre-sized dimensions consisting of active phase most often non-homogeneously dispersed in binder(s).[11] The overall aim is to obtain the required mechanical strength to resist attrition loss, maintain chemical stability for prolonged use and limit expenditure (among many others), whilst achieving high catalytic activity and selectivity. Limited academic knowledge exists in the details of these commercial catalysts. Unlike bulk or supported active-phase catalysts predominately used in academic research, industrial catalysts involve complex physical and chemical interactions between two or more component phases. The choice of binder(s), combined with the formulation method, can severely impact the material's catalytic properties.[12] The role of the selected binder is particularly lacking in understanding and is often incorrectly labelled "inert". Zeolite–binder interactions induced upon the formulation process have a substantial impact on the activity, selectivity and stability of the working catalyst.

A recent perspective by Hargreaves and Munnoch highlights the importance of binder effects that occur in such zeolite-based materials, including modification of coking characteristics, poison entrapment, transfer of chemical species, as well as physical property enhancements.[13] Silica and alumina are inexpensive inorganic binders commonly employed in catalyst bodies.[14–19] Although SiO_2 lacks acid sites able to partake in acid-catalyzed processes, its intimate contact with impregnated zeolite can induce solid-state ion exchange, with Michels et al. and Lee et al. reporting loss of Brønsted acidity as a result of dealumination from the zeolite framework.[17,18] Although the determination of acid sites present in Al_2O_3 binder is less obvious, effects such as aluminium migration from the binder material to the zeolite framework is reported, creating an increase in inter- and/or intra-crystalline acidity, which affects the overall catalytic activity and selectivity.[14]

One of the main contributions to the lack of academic interest in zeolite-based catalyst bodies is the inability to study in detail these large-scale materials with high enough spatiotem-

[a] Dr. G. T. Whiting, Dr. F. Meirer, Prof. B. M. Weckhuysen
Inorganic Chemistry and Catalysis Group
Debye Institute for Nanomaterials Science
Utrecht University
Universiteitsweg 99
3584 CG, Utrecht (The Netherlands)
E-mail: B.M.Weckhuysen@uu.nl

[b] Dr. M. M. Mertens
ExxonMobil Process Technology
ExxonMobil Research and Engineering Company
1545 Route 22 East
Annandale, NJ 08801 (USA)

[c] Dr. A.-J. Bons, Dr. E. de Smit
ExxonMobil Chemical Europe, Inc.
European Technology Centre
Hermeslaan 2
B-1831, Machelen (Belgium)

[d] Dr. B. M. Weiss, Dr. P. A. Stevens
Corporate Strategic Research
ExxonMobil Research and Engineering Company
1545 Route 22 East Annandale
NJ 08801 (USA)

Supporting information for this article is available on the WWW under http://dx.doi.org/10.1002/cctc.201402897.

poral resolution, owing to the reduced field-of-view required and the lack of suitable characterisation techniques available.[12,20,21] Given the recent enhancements in chemical imaging methods,[22,23] such as single-molecule and confocal fluorescence microscopy,[21,24–27] UV/Vis microspectroscopy,[28,29] IR and Raman microscopy,[30–32] transmission soft and hard X-ray microscopy,[33–36] X-ray diffraction computed tomography[37] and focused-ion-beam scanning electron microscopy,[38] coupled with the improved control of these commercial catalysts for modern-day processes,[39] the time is ripe for a shift in academic focus towards understanding these more complex multicomponent and hierarchically structured catalyst materials.

The combination of UV/Vis microspectroscopy and confocal fluorescence microspectroscopy (CFM) have been used recently with remarkable spatiotemporal resolution to investigate Brønsted acid properties in micrometre-sized fluid catalytic cracking (FCC) particles[29,40–43] and more recently millimetre-sized ZSM-5-containing binder-bound extrudates.[44,45] By staining these materials with a probe molecule such as thiophene and following the formation of fluorescent oligomer species in situ, their location, distribution and selectivity provide valuable information on the strength and density of acid sites present. Owing to the specific absorption wavelengths of each light-absorbing oligomer species, laser-line wavelengths in close proximity can be used to selectively excite one or more fluorescent species, which creates a 2D/3D chemical map.

In the work herein, two series of ZSM-5-containing SiO_2- and Al_2O_3-bound millimetre-sized extrudates (with varying active-phase content) were investigated with UV/Vis microspectroscopy and CFM. Furthermore, microcrystalline silicalite-based Al_2O_3-bound samples were studied to confirm possible aluminium migration. By employing thiophene oligomerisation as a selective probe reaction for Brønsted acidity, catalytic activity and selectivity were determined for each sample and related to their physicochemical properties. The variations in selectivity, location and distribution of fluorescent oligomer species (originating on Brønsted acid sites) between SiO_2- and Al_2O_3-bound samples were visualised non-invasively in three dimensions, with a view to establishing binder effects that occur with high spatiotemporal resolution.

Results

Standard characterisation of the catalyst materials

Elemental analysis was used to determine the extent of partial proton exchange in both SiO_2- and Al_2O_3-bound Na–ZSM-5-containing extrudates. As shown in Table 1, the Na content remaining in each extrudate was similar for both binder types (i.e., a linear increase with ZSM-5 content), therefore, the number of Brønsted acid sites present is comparable between each series.

To measure the BET surface area and pore-volume distribution of both series of extrudates, N_2 physisorption was employed. As expected, an increase in binder content corresponded with a decrease in BET surface area, typically associated with a dilution of the zeolite content (Table 1). Furthermore, micropore area and volume also suffer a decline as the active-phase content is reduced. The results of the pore-volume measurements of pure zeolite, pure binder and the mixed-phase extrudates highlight the impact on combining both components during the preparation procedure.

Evidently, the increase in content of both binder types corresponds with an increase in overall pore volume (i.e., the pore volume of Z80-Si, 0.35 $cm^3 g^{-1}$, is smaller than that of Z20-Si, 0.70 $cm^3 g^{-1}$, Table 1). However, the predicted pore volumes (calculation based on those of the pure components) of the ZSM-5:binder-bound extrudates are significantly higher than the experimentally determined ones. Particularly in the case of the SiO_2-bound samples, as much as a 21% decrease was measured for Z20-Si, with the Al_2O_3-bound samples observing the same trend but to a lower extent (Z20-Al, 11% decrease). This exemplifies the changes induced upon combining both the active zeolite phase and the binder material in extrudates, with the decrease in pore volume attributed to blockage/coverage of the binder pores with ZSM-5 crystals/agglomerates and/or morphological changes in the binder. Corresponding pore-size distributions are illustrated in Figure 1. Noticeably, the ZSM-5-based SiO_2-bound extrudates express a far wider pore-size distribution than their Al_2O_3-bound counterparts. An increase in active-phase content creates a narrower pore-size distribution

Table 1. Physicochemical properties of the two series of ZSM-5-containing SiO_2- and Al_2O_3-bound extrudates under investigation.

Sample	ZSM-5:binder [wt.%]	Binder	Na content [ppm]	BET surface area [$m^2 g^{-1}$]	t-plot micropore area [$m^2 g^{-1}$]	Pore volume [$cm^3 g^{-1}$]	t-plot micropore volume [$cm^3 gm^{-1}$]
ZSM-5	100:0	–	–	356	261	0.21	0.13
Z80-Si	80:20	SiO_2	5600	347 (336)[a]	213 (211)	0.35 (0.38)	0.11[b]
Z50-Si	50:50	SiO_2	3690	313 (306)	137 (136)	0.54 (0.64)	0.07
Z20-Si	20:80	SiO_2	1490	255 (275)	59 (61)	0.70 (0.89)	0.03
SiO_2	0:100	SiO_2	–	255	11	1.06	0
Z80-Al	80:20	Al_2O_3	5690	349 (340)	217 (213)	0.28 (0.33)	0.11
Z50-Al	50:50	Al_2O_3	3510	322 (315)	148 (141)	0.45 (0.5)	0.07
Z20-Al	20:80	Al_2O_3	1210	288 (289)	74 (68)	0.60 (0.67)	0.03
Al_2O_3	0:100	Al_2O_3	–	273	20	0.79	0

[a] Predicted values calculated from the extrudate composition and the experimental values of the pure binder and pure zeolite. [b] Predicted micropore volume identical to experimental values.

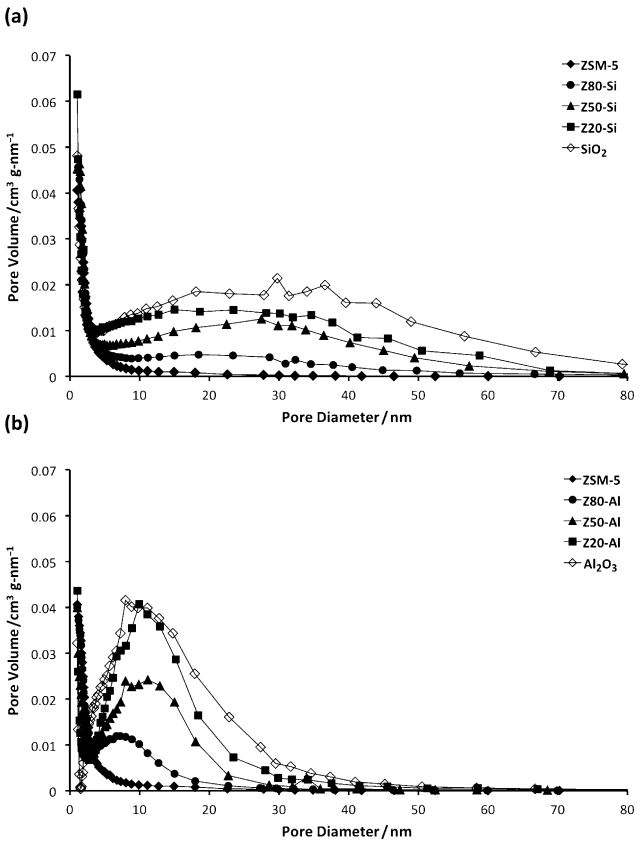

Figure 1. Pore-volume distributions, determined by the Barrett–Joyner–Halenda adsorption method with N_2, for: a) a series of ZSM-5-containing SiO_2-bound extrudates and b) a series of ZSM-5-containing Al_2O_3-bound extrudates.

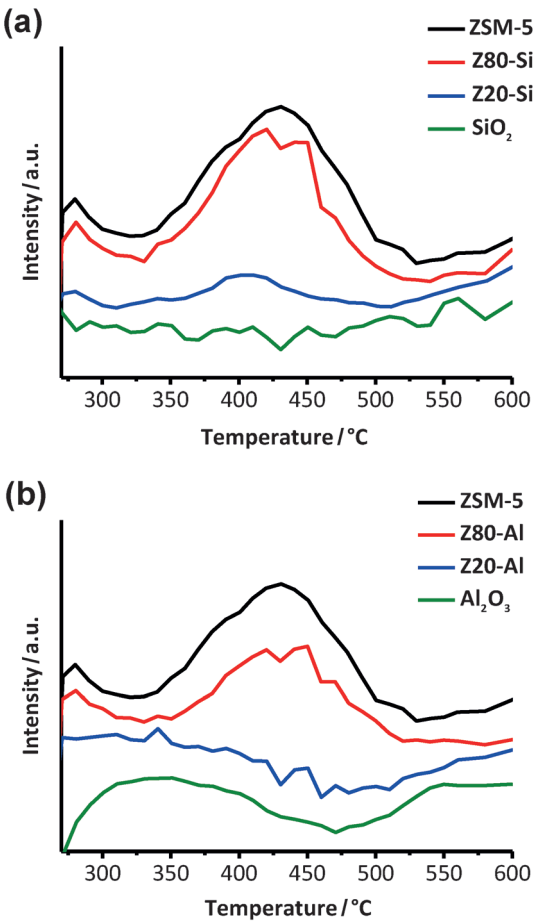

Figure 2. TPD profiles of NH_3 for: a) a series of ZSM-5-containing SiO_2-bound extrudates and b) a series of ZSM-5-containing Al_2O_3-bound extrudates.

in both cases, owing to the lower contribution of mesopores from the decreased binder content.

Concerning the difference in pore-size distribution and pore volume of the SiO_2- and Al_2O_3-bound extrudates, their adsorption capacities were determined by using *n*-hexane adsorption. In Table S1 in the Supporting Information, the experimental values are presented, which clearly display the higher capacity of Al_2O_3-bound ZSM-5-containing extrudates in comparison to that of their corresponding SiO_2-bound extrudates. Measured values correspond well with predicted values (based on pure component measurements), with the ZSM-5 crystals completely accessible.

In Figure 2 the NH_3-temperature programmed desorption (TPD) profiles of both series of ZSM-5-based binder-bound extrudates are shown, with Table S1 presenting the amounts of NH_3 desorbed for each sample. As expected, ZSM-5 crystals produce a broad band centred at 430 °C, attributed with NH_3 desorbing from strong acid sites.[46] A small peak at 270 °C is associated with physisorbed NH_3. Owing to the lack of acid sites in SiO_2, Z80-Si experiences no significant change relative to that of ZSM-5 (Figure 2a), however, the large dilution of the active phase in Z20-Si substantially decreases the amount of NH_3 desorbed on the limited strong acid sites present. The NH_3–TPD profile of Z80-Al (Figure 2b) is similar to that of Z80-Si, however, the peak maximum, associated with strong acid sites is shifted slightly to higher temperatures. The dilution of the active phase in Z20-Al produces a dramatic decrease in strong acid sites, with the peak maximum now shifted significantly to the left (340 °C). This behaviour corresponds well with the NH_3-TPD profile of pure Al_2O_3, which produces a broad band centred at 346 °C, showing that Al_2O_3, unlike SiO_2, cannot be considered an "inert" binder, considering the high contribution towards the extrudates' overall acidity.

The morphology and distribution of ZSM-5 crystals in SiO_2 and Al_2O_3-bound extrudates as assessed with SEM is illustrated in Figure S1 in the Supporting Information. The crystal/agglomerate size of ZSM-5 is in the range of 2–6 μm (Figure S1a). If viewing such small sections of the extrudates, conclusions on the distribution of the active phase in the binder should be drawn with care. However, it can be seen, particularly for Z50-Si and Z50-Al (Figure S1d and e), that Al_2O_3 covers the crystals more homogeneously than SiO_2, creating a "blanket" between crystals.

Probing binder effects with microspectroscopy

The selective staining of Brønsted acid sites in a non-invasive manner has recently been used to study catalyst bodies, such as FCC particles[40,47] and ZSM-5-containing SiO_2-bound extru-

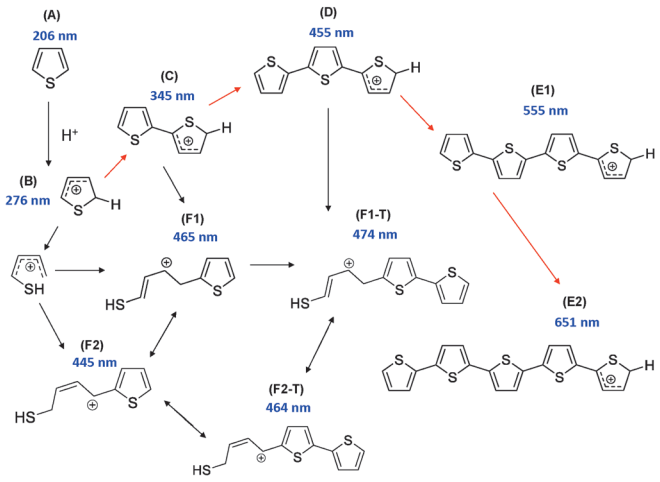

Scheme 1. Proposed reaction pathway of thiophene oligomerisation on zeolite acid sites. Thiophene monomer (**A**) undergoes protonation on Brønsted acid sites of H–ZSM-5 crystals to form the protonated monomer (**B**). Two different reaction pathways are possible at this stage: opening of the thiophene ring and subsequent reaction with a second monomer to form a thiol-like carbocation (**F1**/**F1-T**/**F2**/**F2-T**). Alternatively, dimerisation (to **C**) can occur followed by further oligomerisation (to **D**) or opening of the thiophene ring, forming a thiol-like carbocation (**F1**/**F1-T**/**F2**/**F2-T**). The trimeric carbocationic species (**D**) can undergo further oligomerisation to form more extended/conjugated species (**E1**/**E2**).

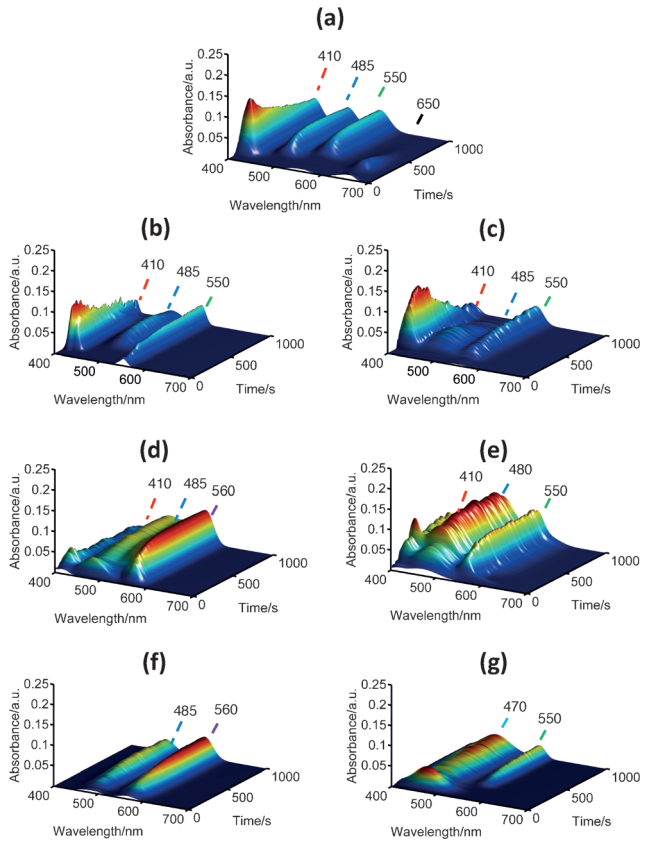

Figure 3. Filtered in situ optical absorption time series spectra (using peak fitting and multivariate analysis) during thiophene oligomerisation over: a) ZSM-5 pellet, b) Z80-Si, c) Z80-Al, d) Z50-Si, e) Z50-Al, f) Z20-Si and g) Z20-Al. Samples were impregnated at 30 °C before applying a temperature ramp (at 30 °C min^{-1}) to 120 °C and spectra were recorded every 10 s for a total of 1000 s.

dates.[44] Herein we employed thiophene oligomerisation as a probe molecule reaction to study Brønsted acidity variations and binder effects between both ZSM-5-containing SiO_2- and Al_2O_3-bound extrudates. As seen in Scheme 1, several carbocations are formed and evidently two reaction pathways take place upon the adsorption and protonation of thiophene monomers: either progressive oligomerisation to form larger more conjugated/extended oligomers (compounds **C**, **D**, **E**) or ring opening to form thiol-like species (**F** compounds). In Figure 3a, the in situ optical absorption spectra (400–700 nm) of a pure ZSM-5 pellet reacted with thiophene are shown. Owing to the complex nature of the raw absorption spectra obtained (Figure S2), multivariate analysis and time-dependent density functional theory calculations (on non-confined molecules) were performed. These were used to fit and tentatively assign the bands formed for each sample's optical spectra, with the background selectively removed. This procedure and more details can be found in our previous work.[44]

Clearly, four bands at 410, 485, 550 and 650 nm are formed over the reaction time. The formation of each band over time is observed with more clarity in Figure S3a. The initial oligomer species formed at 410 nm was assigned to a dimeric and/or trimeric intermediate species. Both the bands at 410 and 650 nm appear to rise and fall at a similar rate, followed in quick succession by the formation of bands at 485 and 550 nm. According to Scheme 1, this is caused by competing reaction pathways, by which the dimeric/trimeric intermediate species undergo both ring opening to form thiol-like species (**F1-T**) and progressive molecular growth (**E1**).

The introduction of SiO_2 binder (Z80-Si) correlates with an initial formation of a four-thiophene ring oligomer (**E1**) (absorption at 550 nm, Figure 3b). Most likely, it is not the first intermediate/product species formed, however, owing to the limitations of the instrument spectral detection range, oligomers absorbing in the UV light region (i.e., **C**) are not detected. The development of both the 410 and 485 nm bands is similar to that of the pure ZSM-5 pellet, for which a decrease in the intensity of the former band is accompanied by an increase in the latter. The time-evolved optical spectra of Z80-Al are shown in Figure 3c. Differing from its corresponding SiO_2 counterpart, three absorption bands at 410, 485 and 550 nm are formed simultaneously at approximately 110 s. Competing reaction pathways (Scheme 1) provide an explanation for this phenomenon, with the progressive molecular growth mechanism becoming dominant as the reaction proceeds.

Both Z50-Si and Z50-Al exhibit significantly increased initial reactivity compared with extrudates containing higher ZSM-5 content. In Figure 3d and e, the optical absorption spectra produced by both Z50-Si and Z50-Al are presented, respectively, with corresponding band formation over time shown in Figure S3d and S3e. The simultaneous formation of 410, 485 and 560 nm bands for the SiO_2-based extrudate is not dissimilar to that of the Al_2O_3-based extrudate, however, noticeably there are slight shifts in both the 485 and 550 nm bands in each

sample. The absorption band at 550 nm associated with the four-thiophene ring species (**E1**) is now present at 560 nm for Z50-Si, and the thiol-like species (**F1-T**), which absorbs light at 485 nm in both pure ZSM-5 and Z80-Al, now present at 480 nm for Z50-Al. These results suggest that the particular carbocationic species are present in an alternate chemical environment in Z50-Si and Z50-Al. However, owing to the complex nature of the thiophene oligomerisation mechanism and the corresponding band assignments of species formed, the formation of other oligomers that absorb light at this wavelength cannot be ruled out.

In terms of oligomer selectivity, Z50-Si exhibits a far higher ratio of more conjugated species (band at 560 nm) versus less conjugated species (410 nm) compared to the ratios displayed by both pure ZSM-5 and Z80-Si (compare Figure 3d with Figure 3a,b). The Al_2O_3-based extrudate on the other hand exhibits higher selectivity towards thiol-like species (absorbing at 480 nm) than Z80-Al (compare Figure 3e with Figure 3c).

This trend, that is, increasing binder content correlates with increasing selectivity towards more extended/conjugated carbocationic species, continues in both Z20-Si and Z20-Al samples. In Figure 3f, the time-resolved optical absorption spectra of Z20-Si during thiophene oligomerisation are shown. Two distinct bands are observed at 485 and 560 nm. The absence of the 410 nm band and the higher intensity of the 560 nm band suggests the further reactivity of the dimeric/trimeric species (410 nm band) towards higher oligomers. The optical absorption spectra produced by Z20-Al (Figure 3g) present a substantially higher selectivity towards ring-opened species (485 nm band) than towards higher oligomers (550 nm band), which differs substantially from the results for the Z20-Si extrudate (Figure 3f). Moreover, the band at 470 nm represents a hypsochromic shift from the band at 480 nm in Z50-Al, indicating the presence of this oligomer species in the binder to a further extent.

Confocal fluorescence microspectroscopy

Upon termination of thiophene oligomerisation performed on ZSM-5-containing SiO_2 and Al_2O_3-bound extrudates, CFM was employed to visualise the distribution of various fluorescent carbocationic species present in two and three dimensions. Excitation of species that absorb light at approximately 485 and approximately 550 nm is possible by using 488 and 561 nm lasers simultaneously. The 3D visualisation of pure ZSM-5 crystals post-reaction is given in Figure S4. All crystals/agglomerates within the field of view are fluorescent (green/yellow), with a select few intensely fluorescent (yellow). This heterogeneous distribution is attributed to the lower amount of Na present in these specific crystals/agglomerates, leading to a higher number of Brønsted acid sites (hence intensely fluorescent crystals).[44] In Figure 4, the 3D top-view volumes of: Z80-Al, Z80-Si; Z50-Al, Z50-Si, Z20-Al, and Z20-Si extrudates are presented. The same heterogeneous distribution of fluorescent intensity can be observed for Z80-Si (Figure 4a) as for pure ZSM-5. As observed in their optical spectra, both pure ZSM-5 crystals (Figure 3a) and Z80-Si (Figure 3b) exhibit a similar intensity of the 485 and 550 nm bands, which correlates with the similar fluorescent intensity/colour. In accordance with the optical spectra of the Z80-Al extrudate (Figure 3c), the orange fluorescence in the CFM image in Figure 4b indicates a higher concentration of more conjugated species (which absorb light at 550 nm) than in the corresponding Z80-Si sample (Figure 4a).

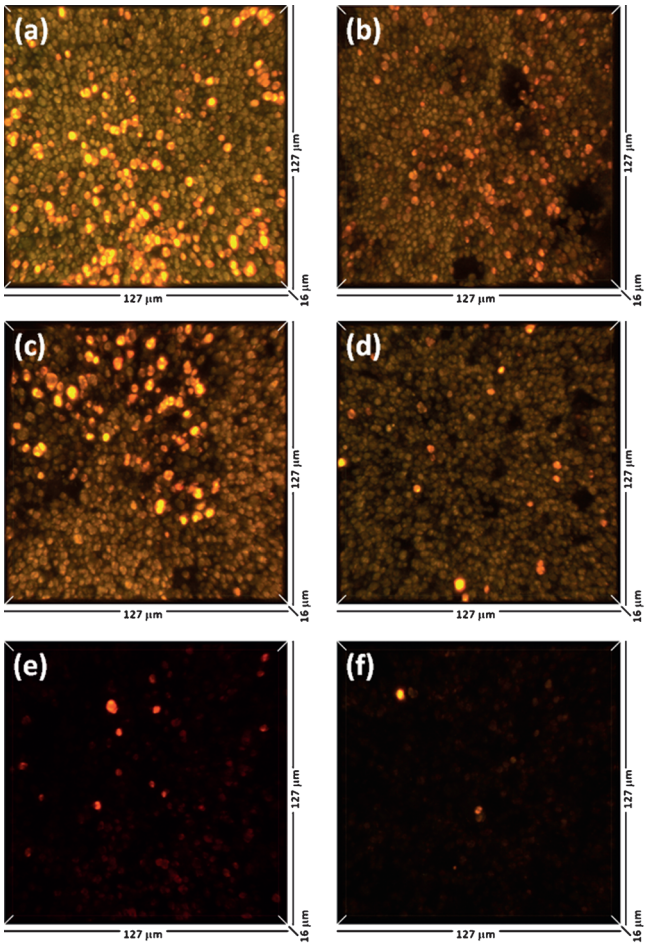

Figure 4. 3D top-view CFM images of a) Z80-Si, b) Z80-Al, c) Z50-Si, d) Z50-Al, e) Z20-Si and f) Z20-Al after thiophene oligomerisation and excited with 488 and 561 nm lasers simultaneously.

A similar trend is observed for both Z50-Si and Z50-Al extrudates (Figure 4c and d, respectively). Again, a heterogeneous distribution exists for both samples, with several crystals/agglomerates more fluorescent than the majority. The higher ratio of the 550–560 nm band versus the 480–485 nm band in the Z50-Si sample (see Figure 3d) can be visualised by its yellow fluorescence produced (Figure 4c). The opposite band intensity ratio was obtained for Z50-Al (see Figure 3e), and this is also displayed by ZSM-5 crystals emitting green/yellow fluorescence (Figure 4d).

The 3D top-view fluorescence images of both Z20-Si and Z20-Al exhibit only a few fluorescent ZSM-5 crystals/agglomerates in the field of view, owing to the limited amount of ZSM-5 present (Figure 4e and f, respectively). However, the higher concentration of more conjugated species present in Z20-Si (see Figure 3f) is displayed by an orange fluorescence. The

yellow fluorescence in Z20-Al correlates well with the higher ratio of less conjugated species, observed in the absorption spectra (see Figure 3g).

Discussion

Establishing the binder effects with microspectroscopy

To understand the differences in activity and selectivity during thiophene oligomerisation between SiO_2- and Al_2O_3-bound ZSM-5-containing extrudates, the physicochemical properties of each material must be taken into consideration. One of the most prominent features in the optical spectra of binder-bound extrudates, in contrast to the spectra of a pure ZSM-5 pellet, is the higher ratio of more conjugated species (compounds **F**/**E**) versus less conjugated species (compounds **C**/**D**). In particular, the 410 nm absorption band associated with dimeric/trimeric species decreases significantly in intensity from Z80-Si Z20-Si (also with Z80-Al, Z20-Al), with a higher ratio of 480 nm and 550 nm bands, attributed to thiol-like (**F1-T**) and four-thiophene ring (**E**) oligomers, respectively. Taking into account the larger pore volume of both ZSM-5-containing SiO_2 and Al_2O_3-bound extrudates in comparison to a pure ZSM-5 pellet (see Table 1), a correlation between the higher number of stored thiophene monomers available per active site and higher reactivity can be made.

Retaining the interest in selectivity variations, it is clear that whether SiO_2 or Al_2O_3 binder is chosen, oligomer selectivity is influenced. It was previously reported that a higher number of Brønsted acid sites present in fully proton-exchanged Na-ZSM-5 SiO_2-bound extrudates favoured the formation of thiol-like species, in contrast to the formation of higher oligomers preferred by corresponding partially proton-exchanged extrudates.[44] Therefore, the acid-site characteristics of samples play a large role in determining the reaction pathway during thiophene oligomerisation.

From the optical absorption spectra of Z50-Si and Z50-Al (Figure 3d and e, respectively), the ratio of the 480–485 to 550–560 nm bands is a significant parameter. These bands are assigned to oligomer species formed through alternate routes during thiophene oligomerisation. For Z50-Si, the higher ratio of the band (550–560 nm) attributed to four-thiophene ring oligomers (**E**) versus the band (480–485 nm) associated with thiol-like species (**F1-T**) is clearly visible. In contrast, Z50-Al has a higher ratio of the thiol-like species (formed via a ring-opening mechanism) versus the higher oligomer species. This feature is further emphasised for both Z20-Si and Z20-Al. From Figure S5, no reactivity for pure SiO_2 extrudates is revealed, with only a limited reactivity of pure Al_2O_3 extrudates.

Therefore, the noticeable change in selectivity between both binder types in extrudates containing ZSM-5 must be caused by physicochemical characteristics induced upon extruding both components. The larger degree of weaker acid sites in Al_2O_3-bound samples in contrast to SiO_2-bound samples (Figure 2, Table S2) might alter the reaction pathway. However, given the limited reactivity of pure Al_2O_3 extrudates, other avenues should be explored.

It is known that the use of Al_2O_3 as a binder if combined with zeolites can lead to aluminium migration from the binder to the surface of the zeolite crystals/zeolite-binder interface, creating additional acid sites.[14–16,47] Therefore, to observe possible aluminium migration and its influence on reactivity, microporous silicalite-based Al_2O_3-bound extrudates Sil80-Al and Sil20-Al (two selected ratios comparable to Z80-Al and Z20-Al) were studied for thiophene oligomerisation. Although silicalite has a near-identical structure to zeolite ZSM-5, its lack of acidity (Table S2) is ideal to study aluminium migration. NH_3–TPD on both Sil80-Al and Sil20-Al revealed the presence of weak acid sites in both extrudates (Table S2, Figure S6). However, with a larger amount of NH_3 adsorbed (0.27 mg g^{-1}) and the higher maximum temperature of desorption (318 °C) in Sil20-Al, a larger number of acid sites are present, with a stronger acidity than in Sil80-Al (0.1 mg g^{-1}, 286 °C).

The optical absorption spectra of Sil80-Al are illustrated in Figure 5a. Strikingly, a relatively high reactivity is obtained, clearly demonstrating that Brønsted acid sites have been formed during preparation. As with the ZSM-5-based extrudates, bands at 410 and 485 nm are formed. However, the absence of a band at 550 nm (compound **E**), coupled with the appearance of a band at 440 nm (**F2**), suggests the favouring of the ring-opening reaction pathway to the further oligomerisation route. In Figure 5b and c, the location of such fluorescent oligomer species formed on acid sites in the silicalite structure in 3D is visualised by using CFM (employing 488 and 561 nm lasers, respectively).

Further investigation of an extrudate containing a higher ratio of Al_2O_3 than silicalite (Sil20-Al), enforces the suspected aluminium migration, with the optical absorption spectra illustrated in Figure 5d. Here, as expected, aluminium migration is observed to a higher extent, with an additional band present at 550 nm displaying the higher reactivity of Sil20-Al compared to Sil80-Al. This higher reactivity is also supported by the higher fluorescence intensity observed if exciting the sample with a 561 nm laser (Figure 5f) compared to that of Sil80-Al (Figure 5c). For both Sil80-Al and Sil20-Al, the higher intensity ratio of thiol-like species bands (440, 485 nm) versus the four-thiophene ring oligomer bands (550 nm) confirms that aluminium migration favours the ring-opening pathway. This binder material effect can explain the higher ratio of thiol-like species formed in ZSM-5-containing Al_2O_3-bound extrudates compared to the one in their corresponding SiO_2-bound extrudates.

Another significant feature of the UV/Vis absorption spectra of binder-bound ZSM-5-containing extrudates, in contrast to the spectra of the pure ZSM-5 pellet, is the absorption-band shifts observed upon thiophene oligomerisation. Hypsochromic (blue shift) or bathochromic (red shift) shifting of bands in the absorption spectra could be caused by the molecules absorbing light at a specific wavelength, interacting with neighbouring molecules different to those present in ZSM-5 pores (i.e., change in chemical environment). In the case of both SiO_2- and Al_2O_3-bound ZSM-5-containing extrudates, hypsochromic/bathochromic band shifts occur and become more apparent with increasing binder content. Whether SiO_2 or Al_2O_3 binder is present determines which absorption bands in

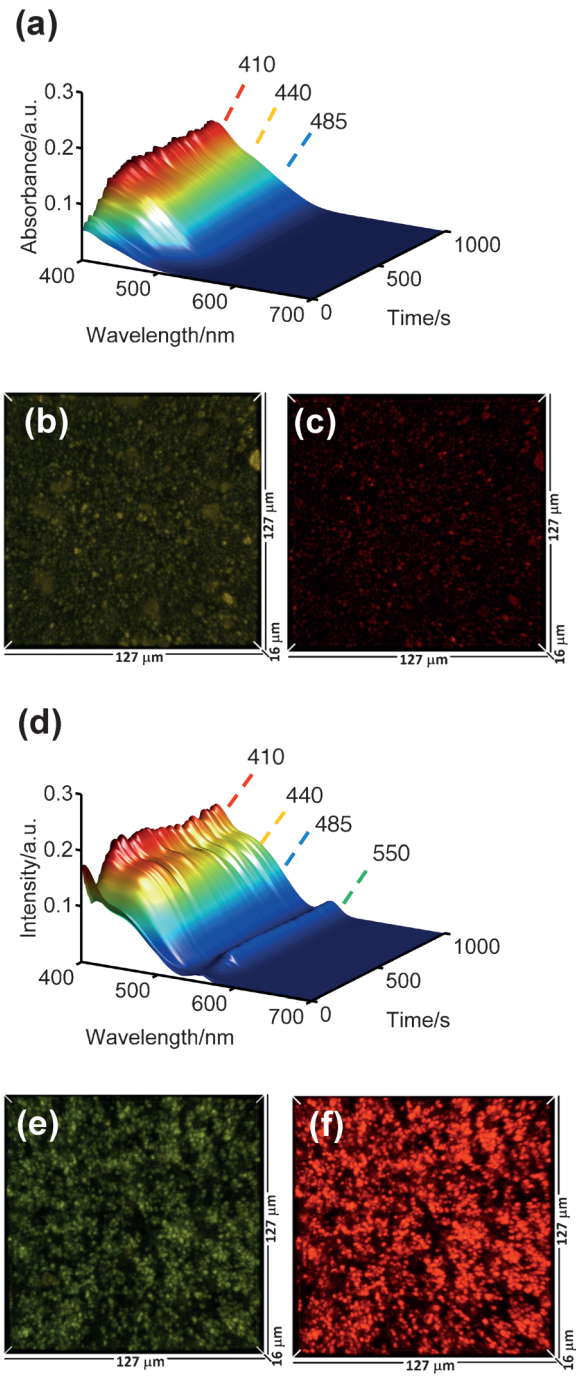

Figure 5. Microspectroscopic analysis of aluminium migration in silicalite-containing Al_2O_3-bound extrudates. a,d) Filtered in situ optical absorption time series spectra during thiophene oligomerisation over Sil80-Al and Sil20-Al, respectively. Corresponding 3D top-view CFM images of b,c) Sil80-Al and e,f) Sil20-Al, excited with b,e) 488 nm laser and c,f) 561 nm laser.

the optical spectra shift, which reinforces the postulation that a change of chemical environment occurs for the molecules in question. For both Z50-Al and Z20-Al, the band originally at 485 nm in Z80-20 hypsochromically shifts to 480 and 470 nm, respectively. This could be the result of the formation of this thiol-like species (**F1-T**) on acid sites created by Al migration, in line with its predominant formation in both Z50-Al and Z20-Al.

In contrast, for Z50-Si and Z20-Si the band attributed to four-thiophene ring oligomers (**E**) bathochromically shifts from 550 to 560 nm. It is highly plausible that these larger molecules grow off the surface of ZSM-5 crystals/agglomerates into the surrounding binder. Evidence of this is visualised by 3D images obtained by CFM and thiophene oligomerisation reaction. In Figure 6a, the 2–6 µm fluorescent green domains are displayed, the locations of which are consistent with the morphology of ZSM-5 crystals/agglomerates (Figure S1a), containing oligomer species (compounds **F**) that absorb light at 488 nm. The additional use of a 561 nm laser (whilst simultaneously employing a 488 nm laser) demonstrates that these larger red fluorescent conjugated/extended species (**E**) appear to grow off the surface of ZSM-5 crystals/agglomerates into the SiO_2 binder (Figure 6b).

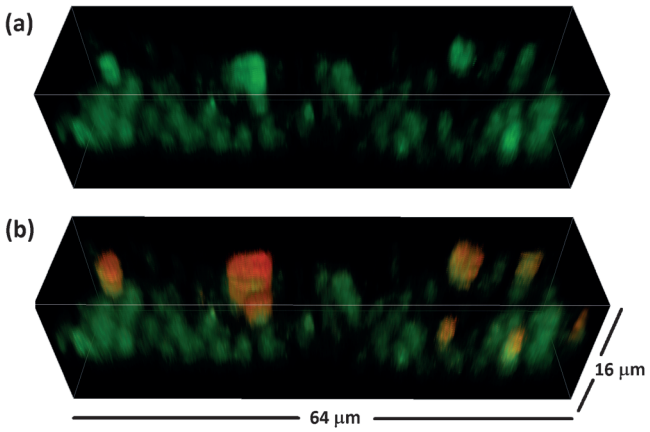

Figure 6. 3D CFM images of a) volume of Z80-Si excited with 488 nm laser, showing fluorescent green oligomers present in ZSM-5 crystals/agglomerates; b) same volume as in (a), excited simultaneously with 488 and 561 nm laser, showing the growth of larger oligomers off the surface of ZSM-5 crystals/agglomerates.

To confirm that the surrounding area of ZSM-5 crystals/agglomerates is indeed binder material, a separate experiment using both thiophene and Nile blue chloride[43] on Z80-Si was performed. Owing to the large molecular dimensions of Nile blue chloride, it is unable to fit inside the zeolite pores and therefore only occupies the binder. By exciting Z80-Si with both 488 and 642 nm lasers, both these compounds can be excited to determine the distribution of active phase and binder. In Figure 7, the location of fluorescent green ZSM-5 domains is illustrated, which are closely surrounded by SiO_2, which emits a red fluorescence. This result confirms the close proximity of the binder material to the ZSM-5 domains, which can allow the growth of oligomer species off the surface of the ZSM-5 crystals into the binder, leading to optical absorption band shifts.

Conclusions

Until recently, establishing binder effects in industrial-scale catalysts such as millimetre-sized extrudates has been based on

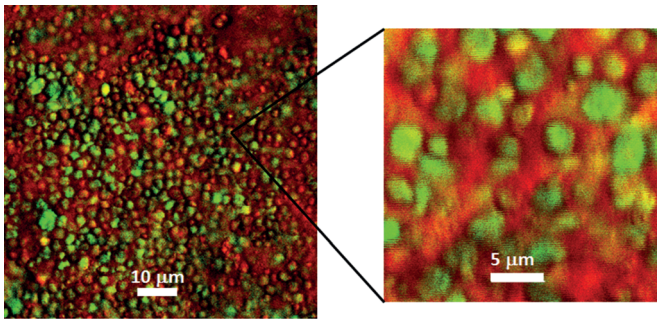

Figure 7. 2D CFM images of Z80-Si reacted with thiophene and impregnated with Nile blue chloride. Simultaneous excitation with 488 and 642 nm lasers produced a green fluorescence attributed to ZSM-5 domains with surrounding binder producing a red fluorescence. Enlargement of the marked area in the left image is shown on the right.

bulk characterisation techniques because of lack of academic research and available techniques able to investigate these complex materials. Herein, advanced non-invasive UV/Vis and confocal fluorescence microspectroscopy, coupled with thiophene as a selective probe for Brønsted acidity, were applied to investigate the binder effects occurring in zeolite ZSM-5-containing SiO_2- and Al_2O_3-bound millimetre-sized extrudates. The selectivity of fluorescent oligomer species located on Brønsted acid sites was found to be dependent on the binder type present. Thiol-like species, obtained through a ring-opening mechanism were predominantly formed on ZSM-5-containing Al_2O_3-bound samples, with corresponding SiO_2-bound samples favouring higher oligomer species. Further studies on microporous silicalite-based Al_2O_3-bound samples confirmed that aluminium migration occurs in Al_2O_3-bound samples, creating Brønsted acid sites that favour the formation of thiol-like species. Moreover, it was found that more conjugated oligomer species appeared to grow off the outer surface of ZSM-5 crystals into the surrounding binder material, which is clearly positioned close by. Evidently, the explored microspectroscopic techniques, in combination with (other) selective probes for, for example, Lewis acid sites, are able to enhance our knowledge of processes occurring in these globally used catalysts, with a view to enhancing process efficiency.

Experimental Section

Extrudate materials

Two series of SiO_2- and Al_2O_3-bound (H-)Na–ZSM-5 containing extrudates were prepared according to patent US6,039,864 (example 1). For the SiO_2-bound extrudates: the required amounts of ZSM-5 crystals, H_2O, SiO_2 gel (AEROSIL 300), silica sol (NALCOAG 1034A) and extrusion aid were mixed prior to extrusion into 2 mm diameter extrudates (Al_2O_3-bound extrudates were prepared by a similar procedure, using Versal 300). Extrudates were dried overnight at 130 °C. Partial ion-exchange was performed after a first calcination (500 °C for 18 h) of the extrudates, by suspending in a 1 M solution of ammonium nitrate for 4 h, followed by washing and drying and a final calcination (500 °C for 18 h). ZSM-5 crystals with a Si/Al ratio of 32 and an average crystal size of 3 μm were used to make silica- and alumina-bound extrudates containing 20 and 80 wt.% of ZSM-5, as summarized in Table 1. Silicalite-based Al_2O_3-bound extrudates were also prepared by a similar method, with the exclusion of Al during silicalite crystal preparation. Extrudate sample notations are as follows: AB-C, in which "A" corresponds to either ZSM-5 ("Z") or silicalite ("Sil") and "B" corresponds to the ZSM-5 or silicalite content (wt.%). Finally, "C" corresponds to SiO_2 bound series ("Si") or the Al_2O_3 bound series ("Al"). As an example: "Z80-Si" is a SiO_2-bound extrudate containing 80 wt.% ZSM-5 crystals.

Elemental analysis

The samples (≈200 mg) were digested in a mixture of acids (30% HCl, 3 mL; 65% HNO_3, 1 mL; 40% HF, 2 mL) for 4–5 h (the first hour with sonication) and then further diluted to 100 mL with purified water from a Merck Milli-Q water system. Further dilution with purified water containing 1% 65% HNO_3 was necessary depending on the expected concentration of the elements to be analysed. Elemental analysis was done with a Varian Vista MPX Inductively Coupled Plasma Optical Emission Spectrometer using multi-element standards provided by Merck and Alfa Aesar.

N_2 physisorption

N_2 physisorption on all samples was performed with an automated gas sorption system Micromeritics TriStar 3000. Prior to measurements, all samples were degassed at 250 °C for 12 h. Surface areas were calculated using by the BET model, whilst external surface area, micropore surface area and micropore volume were determined by using the t-plot method.

Scanning electron microscopy

Extrudates were broken in two, attached to a SEM stub using conductive carbon cement and coated with Pd/Pt in a Cressington 208HR sputter coater. The fracture surface was imaged in a JEOL JSM-6340F Field Emission Gun Scanning Electron Microscope (FEG-SEM) operated at 2 kV using secondary electrons.

Temperature-programmed desorption of NH_3

A Mettler Toledo TGA/SDTA 851 was used to measure adsorption of ammonia at 250 °C followed by desorption under adsorption equilibrium in the temperature range of 250 to 700 °C. After a pre-treatment in air at 500 °C, the samples were exposed to a series of pulses of 1% ammonia in He at 250 °C from which the ammonia adsorption data were generated. Desorption was completed by applying a temperature ramp to 700 °C at 5 °C min^{-1} under 1% ammonia in He flow. All measurement and calculations were weight-based.

Hexane adsorption

The *n*-hexane capacity of the materials was determined by thermogravimetric analysis on a TA Q5000 instrument. The *n*-hexane was delivered with a sparger at a partial pressure of 74 Torr in He. After the samples were pre-treated at 500 °C for 30 min, the *n*-hexane adsorption capacity was measured at 90 °C.

UV/Vis microspectroscopy

Optical microspectroscopy studies were performed in reflectance mode by using an Olympus BX41M upright research microscope, equipped with a 50×0.5 NA objective lens. Illumination of the sample was performed with a 30 W halogen lamp. The microscopy setup was equipped with a 50/50 double-viewport tube, which accommodated a CCD video camera (ColorView IIIu, Soft Imaging System GmbH) and an optical fiber mount. The microscope was connected to a CCD Visible spectrometer (AvaSpec-2048TEC, Avantes) by a 200 μm core fiber. UV/Vis spectroscopy measurements were performed by using an open in situ cell (Linkam Scientific Instruments, FTIR 600) equipped with a temperature controller (Linkam Scientific Instruments TMS 94). All extrudate samples used in the experiment were of similar dimensions (5×1.5 mm), with spectra collected from approximately 5×5 μm areas of each extrudate. Each sample was impregnated with the desired probe molecule solution (5 μL) at 30 °C, before applying a temperature ramp (at 30 °C min^{-1}) to 120 °C. Optical absorption spectra were recorded every 10 s for a total of 1000 s.

Confocal fluorescence microscopy

A Nikon Eclipse 90*i* confocal microscope with a 100×0.73 NA dry objective was used for the fluorescence microscopy investigations. Excitation light was provided by focusing four specific laser lines; 404, 488, 561 and 642 nm on the desired sample, located in an open in situ cell (Linkam Instruments, FTIR 600). The microscope was equipped with a Nikon A1 scan head, accommodating the optics, which couple fibre optics for excitation and emission light with the microscope. A spectral analyser in the Nikon A1 system was equipped with 32 photomultiplier tubes (PMTs) set to collect emission light in the three specific regions depending on the laser line chosen, with a resolution of 6 nm, which were 427–614 nm, 508–697 nm, 581–743 nm, 662–743 nm, corresponding with excitation wavelengths of 404, 488, 561 and 642 nm, respectively. 3D images were recorded at a similar focal depth in each sample by using identical laser power. Prior to microscopic analysis, each sample was impregnated with the desired probe molecule solution (5 μL), before applying a temperature ramp (at 30 °C min^{-1}) to 120 °C, at which temperature the samples were held for 15 min and cooled to 30 °C.

Peak fitting and multivariate analysis

Generally, for each optical absorption data set (100 spectra), principal component analysis was used to determine the number of clusters needed to perform non-negative matrix factorisation (500 000 iterations used). The obtained Eigen spectra were fitted with the minimum number of Gaussians to achieve a good fit ($R^2 >$ 0.99). These Gaussians were then used as a model, to fit each spectra in the time series. Gaussians determined as the background signal were removed, leaving free-standing Gaussians, which provided filtered time-evolved optical absorption spectra.

Acknowledgements

This work was financially supported by ExxonMobil and by a European Research Council (ERC) Advanced Grant (no. 321140) awarded to B.M.W.

Keywords: acidity · fluorescence spectroscopy · microporous materials · sulfur heterocycles · zeolites

[1] A. Corma, *Chem. Rev.* **1995**, *95*, 559–614.
[2] M. J. Climent, A. Corma, S. Iborra, *Chem. Rev.* **2011**, *111*, 1072–1133.
[3] A. Corma, M. J. Díaz-Cabañas, J. Martínez-Triguero, F. Rey, J. Rius, *Nature* **2002**, *418*, 514–517.
[4] W. Vermeiren, J.-P. Gilson, *Top. Catal.* **2009**, *52*, 1131–1161.
[5] C. Marcilly, *J. Catal.* **2003**, *216*, 47–62.
[6] M. Richter, W. Fiebig, H.-G. Jerschkewitz, G. Lischke, G. Öhlmann, *Zeolites* **1989**, *9*, 238–246.
[7] G. Bellussi, P. Pollesel, Molecular Sieves: From Basic Research to Industrial Applications, Proceedings of the 3rd International Zeolite Symposium (3rd FEZA), Elsevier, **2005**.
[8] C. Perego, P. Ingallina, *Catal. Today* **2002**, *73*, 3–22.
[9] J. M. Fougerit, N. S. Gnep, M. Guisnet, P. Amigues, J. L. Duplan, F. Hugues, Zeolites and Related Microporous Materials: State of the Art 1994–Proceedings of the 10th International Zeolite Conference, Garmisch-Partenkirchen, Germany, 17–22 July 1994, Elsevier, **1994**.
[10] D. Shihabi, *J. Catal.* **1985**, *93*, 471–474.
[11] P. A. Jacobs, E. M. Flanigen, J. C. Jansen, H. van Bekkum, *Introduction to Zeolite Science and Practice*, Elsevier, Amsterdam, **2001**.
[12] S. Mitchell, N.-L. Michels, J. Pérez-Ramírez, *Chem. Soc. Rev.* **2013**, *42*, 6094–6112.
[13] J. S. J. Hargreaves, A. L. Munnoch, *Catal. Sci. Technol.* **2013**, *3*, 1165.
[14] M. W. Kasture, P. S. Niphadkar, V. V. Bokade, P. N. Joshi, *Catal. Commun.* **2007**, *8*, 1003–1008.
[15] A. Martin, H. Berndt, U. Lohse, U. Wolf, *J. Chem. Soc. Faraday Trans.* **1993**, *89*, 1277.
[16] Y. Zhang, Y. Zhou, A. Qiu, Y. Wang, Y. Xu, P. Wu, *Ind. Eng. Chem. Res.* **2006**, *45*, 2213–2219.
[17] N.-L. Michels, S. Mitchell, J. Pérez-Ramírez, *ACS Catal.* **2014**, *4*, 2409–2417.
[18] K.-Y. Lee, H.-K. Lee, S.-K. Ihm, *Top. Catal.* **2010**, *53*, 247–253.
[19] P. Sánchez, F. Dorado, A. Fúnez, V. Jiménez, M. J. Ramos, J. L. Valverde, *J. Mol. Catal. A* **2007**, *273*, 109–113.
[20] I. L. C. Buurmans, B. M. Weckhuysen, *Nat. Chem.* **2012**, *4*, 873–886.
[21] M. Kerssens, C. Sprung, G. T. Whiting, B. M. Weckhuysen, *Microporous Mesoporous Mater.* **2014**, *189*, 136–143.
[22] B. M. Weckhuysen, *Angew. Chem. Int. Ed.* **2009**, *48*, 4910–4943; *Angew. Chem.* **2009**, *121*, 5008–5043.
[23] B. M. Weckhuysen, *Chem. Soc. Rev.* **2010**, *39*, 4557–4559.
[24] M. B. J. Roeffaers, B. F. Sels, H. Uji-i, B. Blanpain, P. L'hoëst, P. A. Jacobs, F. C. De Schryver, J. Hofkens, D. E. De Vos, *Angew. Chem. Int. Ed.* **2007**, *46*, 1706–1709; *Angew. Chem.* **2007**, *119*, 1736–1739.
[25] M. B. J. Roeffaers, J. Hofkens, G. De Cremer, F. C. De Schryver, P. A. Jacobs, D. E. De Vos, B. F. Sels, *Catal. Today* **2007**, *126*, 44–53.
[26] P. Chen, X. Zhou, H. Shen, N. M. Andoy, E. Choudhary, K.-S. Han, G. Liu, W. Meng, *Chem. Soc. Rev.* **2010**, *39*, 4560–4570.
[27] G. De Cremer, B. F. Sels, D. E. De Vos, J. Hofkens, M. B. J. Roeffaers, *Chem. Soc. Rev.* **2010**, *39*, 4703–4717.
[28] R. A. Schoonheydt, *Chem. Soc. Rev.* **2010**, *39*, 5051–5066.
[29] J. Ruiz-Martínez, I. L. C. Buurmans, W. V. Knowles, D. van der Beek, J. a. Bergwerff, E. T. C. Vogt, B. M. Weckhuysen, *Appl. Catal. A* **2012**, *419*, 84–94.
[30] E. Stavitski, B. M. Weckhuysen, *Chem. Soc. Rev.* **2010**, *39*, 4615–4625.
[31] E. M. van Schrojenstein Lantman, T. Deckert-Gaudig, A. J. G. Mank, V. Deckert, B. M. Weckhuysen, *Nat. Nanotechnol.* **2012**, *7*, 583–586.
[32] M. W. Zandbergen, S. D. M. Jacques, B. M. Weckhuysen, A. M. Beale, *Angew. Chem. Int. Ed.* **2012**, *51*, 957–960; *Angew. Chem.* **2012**, *124*, 981–984.
[33] Z. Ristanović, B. M. Weckhuysen, *Angew. Chem. Int. Ed.* **2014**, *53*, 8556–8558.
[34] J.-D. Grunwaldt, C. G. Schroer, *Chem. Soc. Rev.* **2010**, *39*, 4741–4753.
[35] J. Ruiz-Martínez, A. M. Beale, U. Deka, M. G. O'Brien, P. D. Quinn, J. F. W. Mosselmans, B. M. Weckhuysen, *Angew. Chem. Int. Ed.* **2013**, *52*, 5983–5987; *Angew. Chem.* **2013**, *125*, 6099–6103.
[36] A. M. Beale, S. D. M. Jacques, B. M. Weckhuysen, *Chem. Soc. Rev.* **2010**, *39*, 4656–4672.

[37] S. D. M. Jacques, M. Di Michiel, A. M. Beale, T. Sochi, M. G. O'Brien, L. Espinosa-Alonso, B. M. Weckhuysen, P. Barnes, *Angew. Chem. Int. Ed.* **2011**, *50*, 10148 – 10152; *Angew. Chem.* **2011**, *123*, 10330 – 10334.
[38] L. Karwacki, D. A. M. de Winter, L. R. Aramburo, M. N. Lebbink, J. A. Post, M. R. Drury, B. M. Weckhuysen, *Angew. Chem. Int. Ed.* **2011**, *50*, 1294 – 1298; *Angew. Chem.* **2011**, *123*, 1330 – 1334.
[39] H. Zhang, R. Xiao, D. Wang, Z. Zhong, M. Song, Q. Pan, G. He, *Energy Fuels* **2009**, *23*, 6199 – 6206.
[40] C. Sprung, B. M. Weckhuysen, *Chem. Eur. J.* **2014**, *20*, 3667 – 3677.
[41] I. L. C. Buurmans, F. Soulimani, J. Ruiz-Martínez, H. E. van der Bij, B. M. Weckhuysen, *Microporous Mesoporous Mater.* **2013**, *166*, 86 – 92.
[42] I. L. C. Buurmans, J. Ruiz-Martínez, S. L. van Leeuwen, D. van der Beek, J. A. Bergwerff, W. V. Knowles, E. T. C. Vogt, B. M. Weckhuysen, *Chem. Eur. J.* **2012**, *18*, 1094 – 1101.
[43] I. L. C. Buurmans, J. Ruiz-Martínez, W. V. Knowles, D. van der Beek, J. A. Bergwerff, E. T. C. Vogt, B. M. Weckhuysen, *Nat. Chem.* **2011**, *3*, 862 – 867.
[44] G. T. Whiting, F. Meirer, D. Valencia, M. M. Mertens, A.-J. Bons, B. M. Weiss, P. A. Stevens, E. De Smit, B. Weckhuysen, *Phys. Chem. Chem. Phys.* **2014**, *16*, 21531 – 21542.
[45] P. Castaño, J. Ruiz-Martínez, E. Epelde, A. G. Gayubo, B. M. Weckhuysen, *ChemCatChem* **2013**, *5*, 2827 – 2831.
[46] J. G. Post, J. H. C. van Hooff, *Zeolites* **1984**, *4*, 9 – 14.
[47] R. V. Jasra, B. Tyagi, Y. M. Badheka, V. N. Choudary, T. S. G. Bhat, *Ind. Eng. Chem. Res.* **2003**, *42*, 3263 – 3272.

Received: November 7, 2014
Published online on January 28, 2015